

AD-A154 249

INTERFEROMETRIC CREEP TESTING(U) AEROSPACE CORP EL
SEGUNDO CA MATERIALS SCIENCES LAB E G WOLFF ET AL.
01 MAR 85 TR-0084A(5935-08)-1 5D-TR-85-02

1/1

UNCLASSIFIED

F04701-83-C-0084

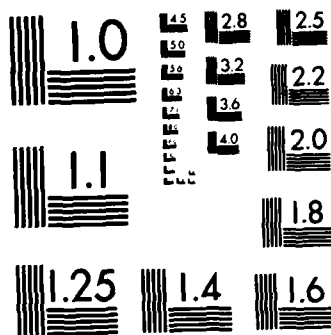
F/G 14/2

NL

END

TABLE 1

DTIC



MICROCOPY RESOLUTION TEST CHART
NATIONAL BUREAU OF STANDARDS-1963-A

AD-A154 249

Interferometric Creep Testing

E. G. WOLFF, R. C. SAVEDRA, and D. J. CHANG
Materials Sciences Laboratory
Laboratory Operations
The Aerospace Corporation
El Segundo, CA 90245

1 March 1985

DTIC
ELECTE
MAY 30 1985

APPROVED FOR PUBLIC RELEASE;
DISTRIBUTION UNLIMITED

B

DTIC FILE COPY


Prepared for
SPACE DIVISION
AIR FORCE SYSTEMS COMMAND
Los Angeles Air Force Station
P.O. Box 92960, Worldway Postal Center
Los Angeles, CA 90009-2960

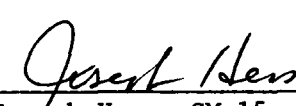
25 7

This report was submitted by The Aerospace Corporation, El Segundo, CA 90245, under Contract No. F04701-83-C-0084 with the Space Division, P.O. Box 92960, Worldway Postal Center, Los Angeles, CA 90009-2960. It was reviewed and approved for The Aerospace Corporation by Louis R. McCreight, Director, Materials Sciences Laboratory. Captain Stephen H. Doerr, SD/YUE, was the project officer for the Mission-Oriented Investigation and Experimentation (MOIE) program.

This report has been reviewed by the Public Affairs Office (PAS) and is releasable to the National Technical Information Service (NTIS). At NTIS, it will be available to the general public, including foreign nationals.

This technical report has been reviewed and is approved for publication. Publication of this report does not constitute Air Force approval of the report's findings or conclusions. It is published only for the exchange and stimulation of ideas.


Stephen H. Doerr, Captain, USAF
Project Officer


Joseph Hess, GM-15, Director, West Coast
Office, AF Space Technology Center

UNCLASSIFIED

SECURITY CLASSIFICATION OF THIS PAGE (When Data Entered)

REPORT DOCUMENTATION PAGE		READ INSTRUCTIONS BEFORE COMPLETING FORM
1. REPORT NUMBER SD-TR-85-02	2. GOVT ACCESSION NO. A154249	3. REPORT'S CATALOG NUMBER
4. TITLE (and Subtitle) INTERFEROMETRIC CREEP TESTING		5. TYPE OF REPORT & PERIOD COVERED
7. AUTHOR(s) E. G. Wolff, R. C. Savedra, and D. J. Chang		6. PERFORMING ORG. REPORT NUMBER TR-0084A(5935-08)-1
9. PERFORMING ORGANIZATION NAME AND ADDRESS The Aerospace Corporation El Segundo, CA 90245		8. CONTRACT OR GRANT NUMBER(s) F04701-83-C-0084
11. CONTROLLING OFFICE NAME AND ADDRESS Space Division Los Angeles Air Force Station Los Angeles, CA 90009-2960		10. PROGRAM ELEMENT, PROJECT, TASK AREA & WORK UNIT NUMBERS
14. MONITORING AGENCY NAME & ADDRESS (if different from Controlling Office)		12. REPORT DATE 1 March 1985
		13. NUMBER OF PAGES 39
		15. SECURITY CLASS. (of this report) Unclassified
		15a. DECLASSIFICATION/DOWNGRADING SCHEDULE
16. DISTRIBUTION STATEMENT (of this Report) Approved for public release; distribution unlimited.		
17. DISTRIBUTION STATEMENT (of the abstract entered in Block 20, if different from Report)		
18. SUPPLEMENTARY NOTES		
19. KEY WORDS (Continue on reverse side if necessary and identify by block number) Creep, Compression testing Interferometry, Michelson Metrology, Fabry-Perot Dimensional stability,		
20. ABSTRACT (Continue on reverse side if necessary and identify by block number) Compressive microcreep data are increasingly needed for the design of dimensionally stable components and structures. Interferometers are inherently more accurate for such measurements than conventional gages or transducers. Described is work with Fabry-Perot and Michelson interferometers that led to development of a novel technique applicable to a wide variety of temperature and loading conditions. A finite-element analysis was performed to analyze loading effects on the accuracy of the optical measurements. Preliminary testing with the device indicates a strain sensitivity of about 2 parts in		

DD FORM 1473
(FACSIMILE)UNCLASSIFIED
SECURITY CLASSIFICATION OF THIS PAGE (When Data Entered)

UNCLASSIFIED

SECURITY CLASSIFICATION OF THIS PAGE(When Data Entered)

19. KEY WORDS (Continued)

Handwritten: 1. 10⁻⁶ to 10⁻⁸ in.
- + 10⁻⁶ in.

20. ABSTRACT (Continued)

10⁹, a strain measurement accuracy of ± 1.2 parts in 10^8 , and a system drift rate of < 1 part in 10^7 /100 hr. Under creep conditions, short-term strains will be a result almost entirely of fluctuations in test-sample temperature.

Handwritten: 1. 10⁻⁶ to 10⁻⁸ in.

Handwritten: 1. 10⁻⁶ to 10⁻⁸ in.

UNCLASSIFIED

SECURITY CLASSIFICATION OF THIS PAGE(When Data Entered)

CONTENTS

I.	INTRODUCTION.....	5
A.	Objective.....	5
B.	Background.....	5
C.	Scope.....	6
II.	TECHNIQUE SELECTION.....	7
A.	Fabry-Perot Interferometer.....	7
B.	Michelson Interferometer.....	7
III.	DESIGN OF A NEW SYSTEM.....	15
A.	Load Application.....	15
B.	Optical System.....	15
IV.	ERROR ANALYSIS.....	19
A.	Optical Errors.....	19
B.	Mechanical System Errors.....	19
1.	Creep Effects.....	19
2.	Asymmetrical Loading.....	30
C.	Signal-Processing Errors.....	34
D.	Thermal Errors.....	35
V.	CONCLUSIONS.....	39
	REFERENCES.....	41

DTIC
ELECTE
MAY 30 1985
B



Accession For	
NTIS GRA&I	<input checked="" type="checkbox"/>
DTIC TAB	<input type="checkbox"/>
Unannounced	<input type="checkbox"/>
Justification	
By	
Distribution/	
Availability Codes	
Dist	Avail and/or Special
A-1	

FIGURES

1.	Fabry-Perot interferometer for compression creep testing.....	8
2.	Effect of optical pathlength difference (OPLD) on the stability in air of a Michelson interferometer.....	10
3.	Indirectly loaded compression creep fixture with a Michelson interferometer strain transducer.....	11
4.	(a) Stability data for the creep test arrangement of Figure 3, with a pressure of 6000 psi on a 5-in.-diam alumina rod. (b) Stability data when both mirrors (D and B) were mounted on top plate during compression test. (c) Stability data when both mirrors (D and B) were mounted on lower sample support plate.....	13
5.	Photograph of new creep test system showing lead-brick loading system and modulated photodetector output signals.....	16
6.	New creep test system with Michelson interferometry.....	17
7.	Finite-element model for analysis of test cylinder and steel plate-mirror interaction under normal compression.....	21
8.	Typical bilinear stress-strain curve.....	22
9.	Cylinder-substrate-steel plate interaction under normal load.....	24
10.	Displacement difference between elastic and inelastic analyses for the cylinder-substrate-steel plate interaction under normal load ($\alpha = 0.95$).....	25
11.	Compressive stress at specimen-plate interface.....	26
12.	Normal compressive stress as a function of axial location (with $\alpha = 0.5$).....	27
13.	Displacement difference between elastic and inelastic cases versus the inelastic strain.....	29
14.	Strain readings from strain gages mounted 180 deg apart on a 0.5-in.-diam Al rod under 1236-lb axial compressions.....	31
15.	Maximum difference in surface σ_z for asymmetrically loaded model system ($\epsilon/\delta = 0.13$).....	33

FIGURES (Continued)

16. Temperature of Zerodur sample and apparent strain as a function of time with PZT-modulated mirror (point b in Figure 6).....	36
17. Temperature of Zerodur sample and apparent strain as measured by quadrature photodetector signals without a PZT-modulated mirror.....	38

TABLE

1. Summary of Cylinder-Substrate-Steel Plate Interaction under Normal Load.....	28
--	----

I. INTRODUCTION

A. OBJECTIVE

The objective of this investigation was to develop an apparatus for creep measurement that incorporates all of the following capabilities simultaneously:

- Constant compressive load of 0 to 2000 lb for >2500 hr in air.
- Constant and uniform sample temperature of 75 to >300°F.
- Continuous creep strain measurement to a resolution of 0.1 μ in./in./decade of time and an accuracy of <1 μ in./in./decade of time.
- Provision for periodic interruptions for room-temperature measurement of net creep strains after arbitrary recovery periods.

The Fabry-Perot and Michelson interferometers are considered to be inherently adaptable to the prescribed conditions. With both methods, the sample end faces, whose relative motion is being measured, either form the active optical elements or can be maintained in close contact with them. Optical phase measurements can readily achieve the required resolution and provide continuous output data. Compressive loads can be applied without interference from the optics. This report describes our work with these configurations to derive a new design.

B. BACKGROUND

Composite materials are increasingly being used to construct dimensionally stable structures, which places new demands on creep (time-dependent, stress-induced strain) measurement techniques. Studies of creep have been dominated by strain gage, extensometer, and capacitance methods.¹⁻³ Such methods cannot achieve accuracies of much better than 1 part in 10^7 , however, because of a variety of factors: strain-gage adhesive stability affects long-term results;¹ gage attachment, nonlinearity, and adiabatic heating or cooling affect capacitance methods;^{2,3} and intermittent methods, for example, gage block comparators, suffer from sample heating/cooling effects, recovery

phenomena, and transient loading effects. Fiber reinforcements tend to reduce the magnitude of creep strains, and there is growing evidence that creep behavior is generally nonlinear. More precise techniques than those now employed could detect early deviations from linear creep and recovery behavior, thereby enhancing long-term predictions.

Laser interferometry, principally Fizeau, Fabry-Perot, and Michelson, has frequently been applied to the measurement of dimensional-stability behavior, such as thermal expansion⁴ and temporal isothermal stability (no applied stress).^{5,6} Such techniques offer real-time strain monitoring to a resolution of $\lambda/1000$ or better, the typical laser wavelength λ being 6328 Å (HeNe). Nonlaser interferometric techniques are less well suited to our objectives. Fizeau and holographic interferometry have been applied to study the inelastic behavior and microcreep of nonmetallic mirror materials,^{3,7} but here surface deformations rather than linear displacements are of primary interest. The Dyson and Hartman-Bennett polarizing interferometers have had considerable difficulties measuring relative changes in length to the order of 5 parts in 10^8 over long times.⁶

C. SCOPE

Preliminary experiments with Fabry-Perot and Michelson interferometers led to a unique design based on the latter. Deadweight axial compressive loading precluded direct laser beam reflection from the sample ends. An alternative optical system is outlined and analyzed for measurement errors. Signal processing and typical performance characteristics are also described with a view toward defining the range of possible applications.

II. TECHNIQUE SELECTION

A. FABRY-PEROT INTERFEROMETER

A Fabry-Perot interferometer, basically an optical resonator, normally consists of a sample spacer or etalon placed between two partially transmitting, nearly parallel mirrors. The resulting multiple-beam interference pattern of the transmitted light is particularly sensitive to changes in the separation of the two mirrors, which can therefore be readily monitored with a photodetector, as shown in Figure 1. Since the multiple reflections occur at exactly the sample ends, thermally induced motions of the optics supports have little effect on the output signal. The $\lambda/2$ and $\lambda/4$ plates are needed to adjust polarization states and serve as optical isolators, because back reflections into the laser cavity generate excessive system noise.

Fabry-Perot fringes are inherently sharp, and alignment is easily achieved; however, there is a high sensitivity to the air path index of refraction n . Sample heating causes convection currents and hence large fluctuations in n . Fabry-Perot interferometers are normally operated in a vacuum for this reason.⁸ Vibrational stability and mechanical creep of optics supports significantly influence the performance of Fabry-Perot interferometers. Since optical and mechanical loading paths are difficult to separate, the design of loading fixtures for sample creep studies is limited. This technique has been developed for temporal stability studies by Professor S. Jacobs at the University of Arizona and would require further development for creep studies of rod samples.

B. MICHELSON INTERFEROMETER

A Michelson interferometer employs a separate beam splitter that sends the two beams to different mirrored surfaces. The reflected beams are directed to recombine at the same beam splitter, and the resulting interference pattern can be detected by photodetectors. Consequently, a Michelson interferometer measures the relative change of two substantial (but preferably equal) optical pathlengths (OPLs), each of which equals the geometrical length

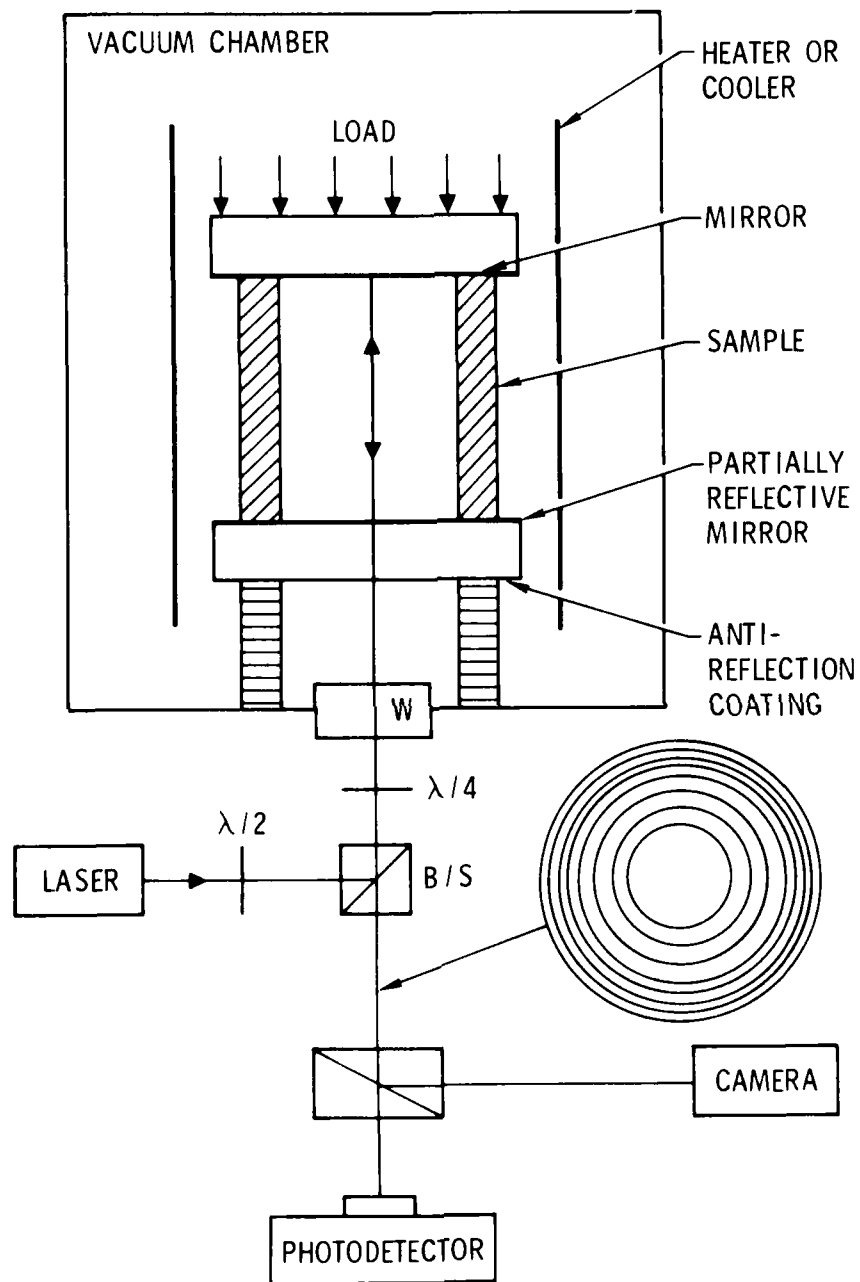


Figure 1. Fabry-Perot interferometer for compression creep testing.

times the index of refraction n . Figure 2 demonstrates the importance of using equal optical pathlengths in air. The interferometer on the left uses two reflecting mirrors in one arm to produce an arbitrarily long path relative to the other arm's. [One of the mirrors is mounted on a piezoelectric transducer (PZT) that is oscillated to help in the fringe counting.] The output trace reflects an apparent change in optical pathlength difference of 20 mV ($\equiv \lambda$) in 20 min, which was caused by changes in the air paths' index of refraction and not mirror motion. With the optical arrangement on the right, the same index of refraction change has no effect, because it acts equally on equal (geometrical) pathlengths. In summary, the system drift under each optical scheme depends on temperature fluctuations, convection currents, and possible compositional changes of the air in one path being compensated for by similar changes in the other. The signal processing used⁹ set 10 mV equal to $\lambda/2$ or 3164 Å (about 12.5 $\mu\text{in.}$).

Figure 3 shows a fixture for applying a compressive stress to a cylindrical sample in a tensile creep frame. The two reflecting mirrors of the Michelson interferometer are glued to the platens that apply the compressive stress to the sample. Phase modulation is a convenient method for determining the direction of the fringe movement and hence sample deformation.⁹ However, the depth of modulation obtainable with conventional PZTs is inadequate for

the incoming beam. The PZT must be placed in one arm of the interferometer, and then equal OPLs are not readily achieved. Based on the literature,^{10,11} a 10°F temperature increase in the air paths in Figure 3, where the difference in OPL was 0.75 in., would be recorded as a 4- $\mu\text{in.}$ sample compression. Again, a change in relative humidity (RH) from 50 to 75% would give an apparent change of 0.3 $\mu\text{in.}$ These potential errors would make long-term stability measurements difficult to interpret, because creep and expected strain instabilities are often of the same order of magnitude.

To minimize such errors, a constant-temperature, constant-humidity room was constructed. Its temperature control was gradually improved from $70 \pm 2^\circ\text{F}$ to $70 \pm 0.25^\circ\text{F}$ (and $50 \pm 5\%$ RH). All apparatus (e.g., Figs. 1 through 3), except the data-recording instruments, were placed in this room.

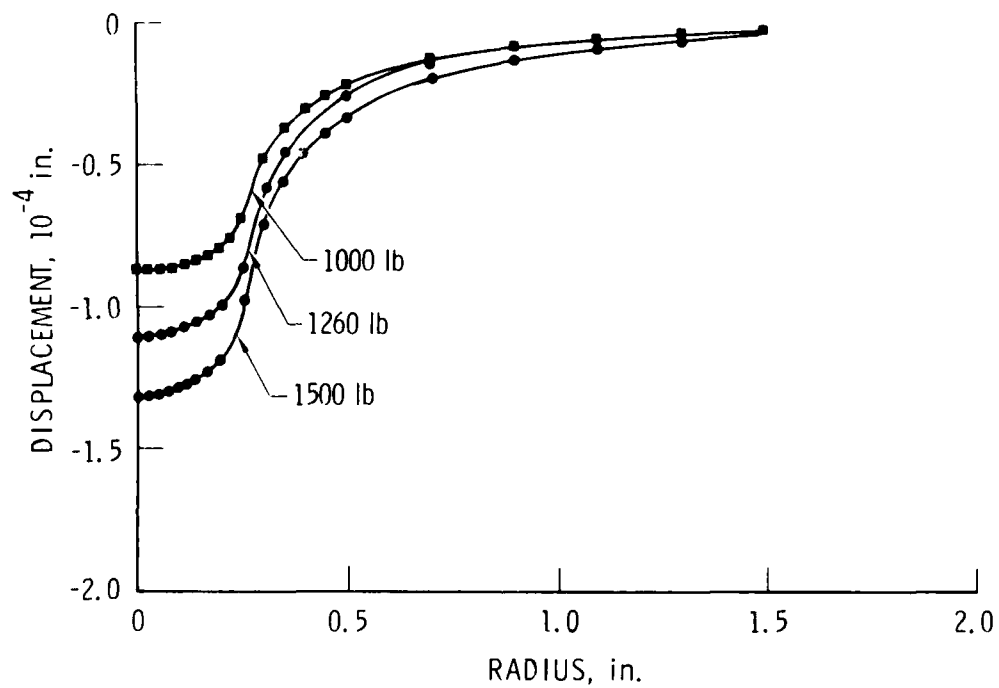


Figure 9. Cylinder-substrate-steel plate interaction under normal load. The displacement occurs in the z-axis. (See Figure 7.)

We analyzed three compressive loads: 1000, 1260, and 1500 lb. The normal displacement (vertical or z-direction) along the mirror surface of either steel plate is shown in Figure 9. The displacement differences between the inelastic and elastic cases are plotted in Figure 10 for $\alpha = 0.95$. Figure 11 shows the corresponding compressive stresses at the sample-plate interface as a function of sample radius for different α 's. The stress at the edge of the sample is very large compared with the average stress. For example, with a uniform load of 1260 lb, the stress at the center of the sample end is 5000 psi and rises at the edges ($R = 0.25$ in.) to about 11,000 psi. However, it exceeds 6000 psi for only about $0.22 < R < 0.25$, or 22% of the total cross-sectional area. Figure 12 illustrates the normal stress in the sample as one leaves the interface at various radial locations. Only the first 0.2 in. from each end has stresses significantly above the average for the entire specimen.

Most of the normal displacement and displacement difference occur at the specimen-stainless steel plate interfaces. The normal displacement at the top of the steel plate away from the specimen decreases rapidly when the radial distance increases. For example, the normal displacement at $r = 0.25$ in. (the edge of the specimen) under a 1260-lb compressive load is -0.8818×10^{-4} in. The normal (or longitudinal) displacement reduces to -0.2793×10^{-4} at $r = 0.5$ in. at the same load level.

The normal displacement difference between the elastic and inelastic cases increases with the increase of inelastic strain, and the displacement differences between inelastic and elastic cases approach infinitesimally small values when the radial distance from the center of the specimen is greater than 0.5 in. Table 1 summarizes the normal displacement fields at different radial stations for different loadings, as well as the maximum normal stresses and inelastic strains at the specimen-stainless steel plate interface. The normal displacement difference between the elastic and inelastic cases can be represented as a function of inelastic strain only and is independent of the magnitude of the applied load. Figure 13 depicts the displacement difference versus inelastic strain at $r = 0.25$ and 0.50 in. The normal displacement difference at $r = 0.50$ in. is approximately one-thirtieth the displacement

Values for α of 0.50 and 0.95 (see Fig. 8) were selected arbitrarily in order to generate plastic strains. Whether one uses plastic strains or creep strains is immaterial because both are inelastic phenomena and, as long as the magnitudes are equal, both will produce exactly the same stress and displacement fields.

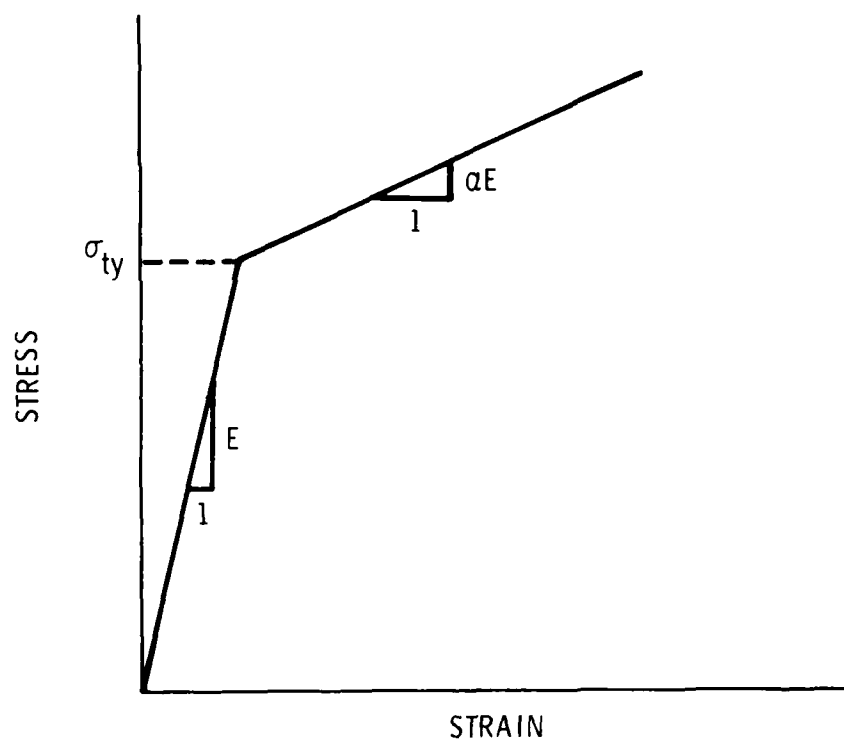


Figure 8. Typical bilinear stress-strain curve. The parameter α is the secant-to-tangent modulus ratio; E is the apparent elastic modulus.

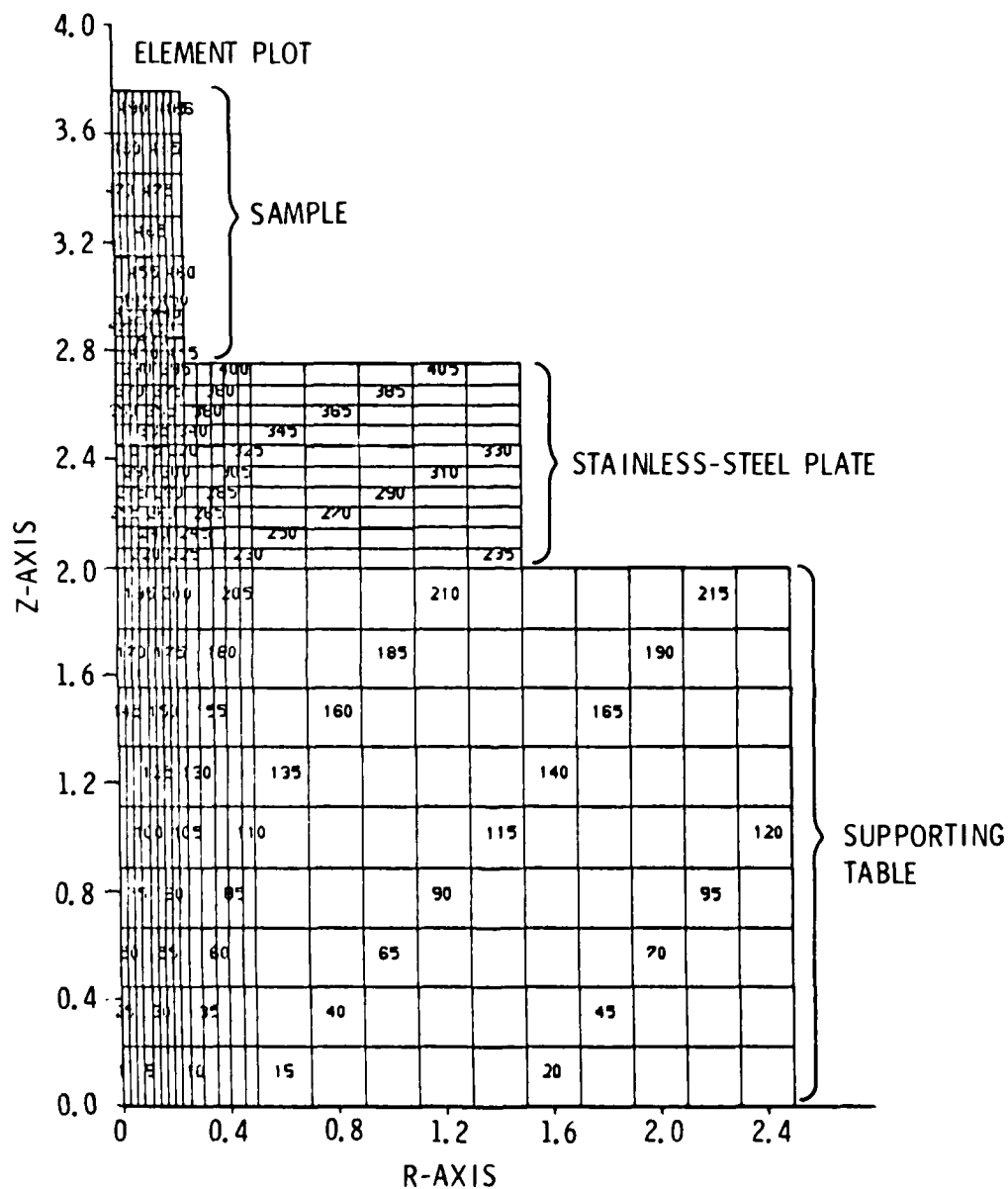


Figure 7. Finite-element model for analysis of test cylinder and steel plate-mirror interaction under normal compression.

When a compressive load is applied to the specimen, the stainless-steel plate at the mounting point is displaced and rotates. When yielding or creep occurs in the specimen, the displacement and rotation at the mounting point change relative to the unyield/uncreep states because of a stress redistribution at the interface between the specimen and the base plate. Consequently, the deformation of the laser interferometer mounting point produces a measurement error in the laser interferometer reading. The displacement change must therefore be determined at the laser interferometer device (point d in Fig. 6) because of the local yielding or creep in the specimen or mirror plates.

For the analysis, we used the Aerospace in-house computer code SAAS III, and specifically the axisymmetric option because the test fixture and specimen were cylindrical. Figure 7 depicts the finite-element model used for the analysis. The cross section of the steel support plate had a 2.5-in. radius and was 2 in. thick. The displacement and stress fields outside that region were considered too small to be significant. The entire structure is simulated by generating the cross section about the axis of revolution. A total of 550 nodes and 496 elements was used to represent the cross section. Fine grid sizes were used in the specimen and regions underneath it. Coarser grid sizes were used for regions away from the center of revolution because the displacements and stresses are smaller and more uniform.

The moduli of elasticity E , Poisson's ratios ν , yield strengths σ_{ty} , and secant-to-tangent modulus ratios α used in the code were as follows:

<u>Stainless Steel</u>	<u>Test Specimen</u>
$E = 29 \times 10^6 \text{ psi}$	$E = 16 \times 10^6 \text{ psi}$
$\nu = 0.33$	$\nu = 0.3$
$\sigma_{ty} = 30,000 \text{ psi}$	$\sigma_{ty} = 5000 \text{ psi}$
$\alpha = 1 \text{ (elastic case)}$	$\alpha = 0.50 \text{ and } 0.95$

IV. ERROR ANALYSIS

Potential errors in the new creep test system may originate from the optical, mechanical, electrical/signal-processing, or thermal subsystems. Each error type is discussed separately below.

A. OPTICAL ERRORS

Optical factors produce errors because of unequal refractive indexes ($n_1 \neq n_2$), as from heater-induced convection; laser motion; vertical motion of the Zerodur prism; and laser frequency stability.

The first problem can be minimized by making the optical pathlengths equal:

$$\overrightarrow{abcd} = \overrightarrow{aef} \quad (3)$$

By surrounding the beam \overrightarrow{cd} with a glass tube, we reduced optically induced signal noise.

No error results when the laser moves vertically if all mirrors are at 45 deg. The lower beam path \overrightarrow{ef} remains constant if the prism moves up or down or if the Zerodur plate expands. (This again requires a 45-deg slope at e.) Since the beam splitter is mounted on the lower steel plate (on a Zerodur block), uniform motion of the steel plate has no effect. The distance \overrightarrow{ae} is minimized to avoid possible bowing errors. Laser frequency stability was 1 part in $10^9/500$ hr with a stabilized Perkin-Elmer HeNe laser. Power levels were about 500 μ W.

B. MECHANICAL SYSTEM ERRORS

1. CREEP EFFECTS

We performed a bilinear finite-element stress analysis to determine the stress and displacement distributions in the microcreep device. The two mirrored plates on each side of the sample were assumed to be 3-in.-diam, 0.75-in.-thick stainless steel.

$$\Delta L_s = \Delta OPLD = \frac{\lambda}{n_{avg}} \left(\Delta N + \frac{\Delta \delta}{2\pi} \right) - \frac{\Delta n_{avg}}{n_{avg}} \quad (2)$$

where n_1 and n_2 represent the indexes of refraction in the two beam paths, λ is the wavelength of HeNe laser light in air, n_{avg} is the average index of refraction in all the beam paths, ΔN is the number of fringes passing a point in space in the beam, and $\Delta \delta$ is the change in phase within a single fringe. The term ΔL_s represents the sample length change. All the surfaces at b, c, d, e, and f are polished and aluminized. The prism for reflections c and d and the optics supports for the beam splitter a and PZT at b are machined from Zerodur blocks (low-thermal-expansion glass ceramics).

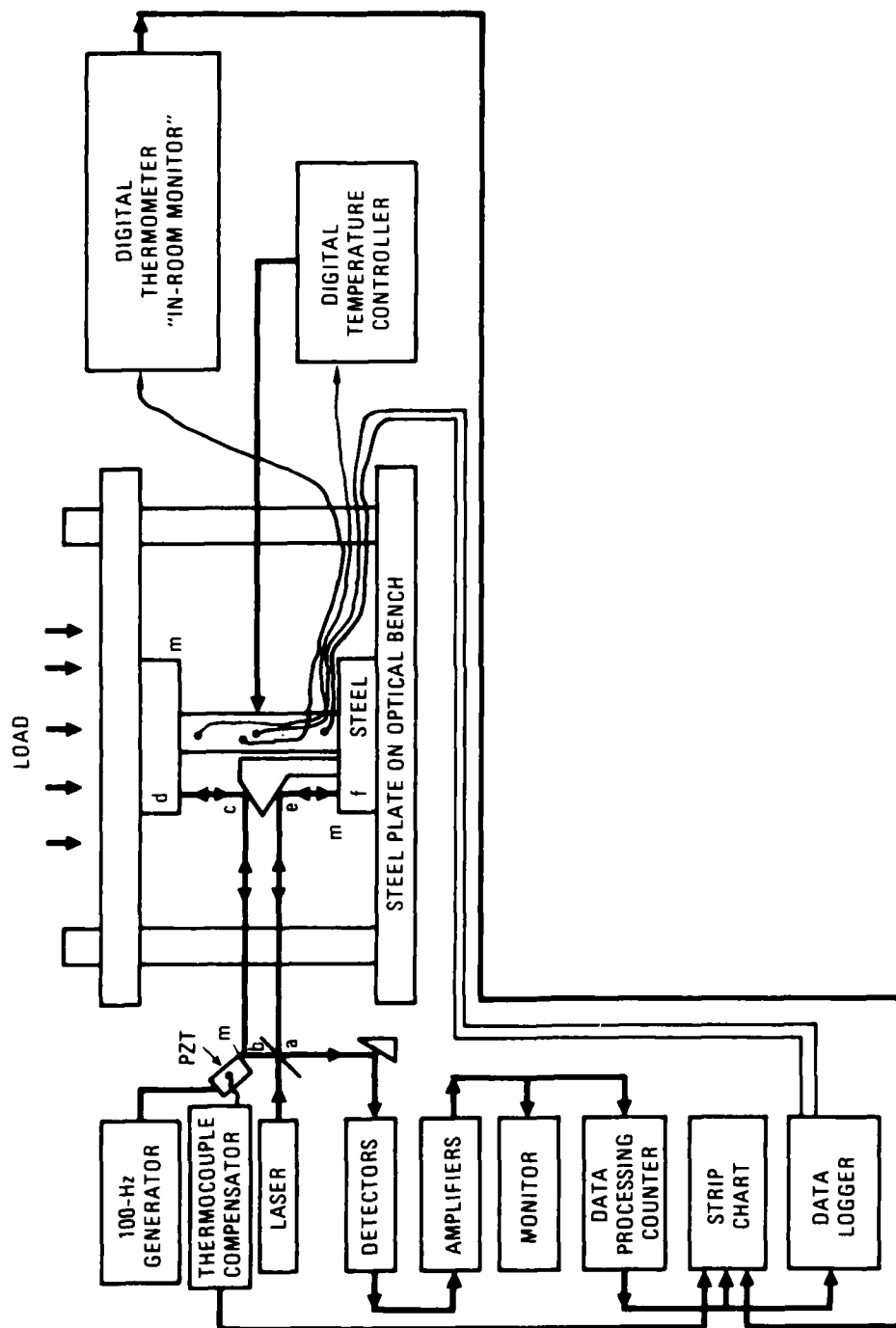


Figure 6. New creep test system with Michelson interferometry. Interferometer arms are aef and abcd. Reflective surfaces e and c are on polished Zerodur block.

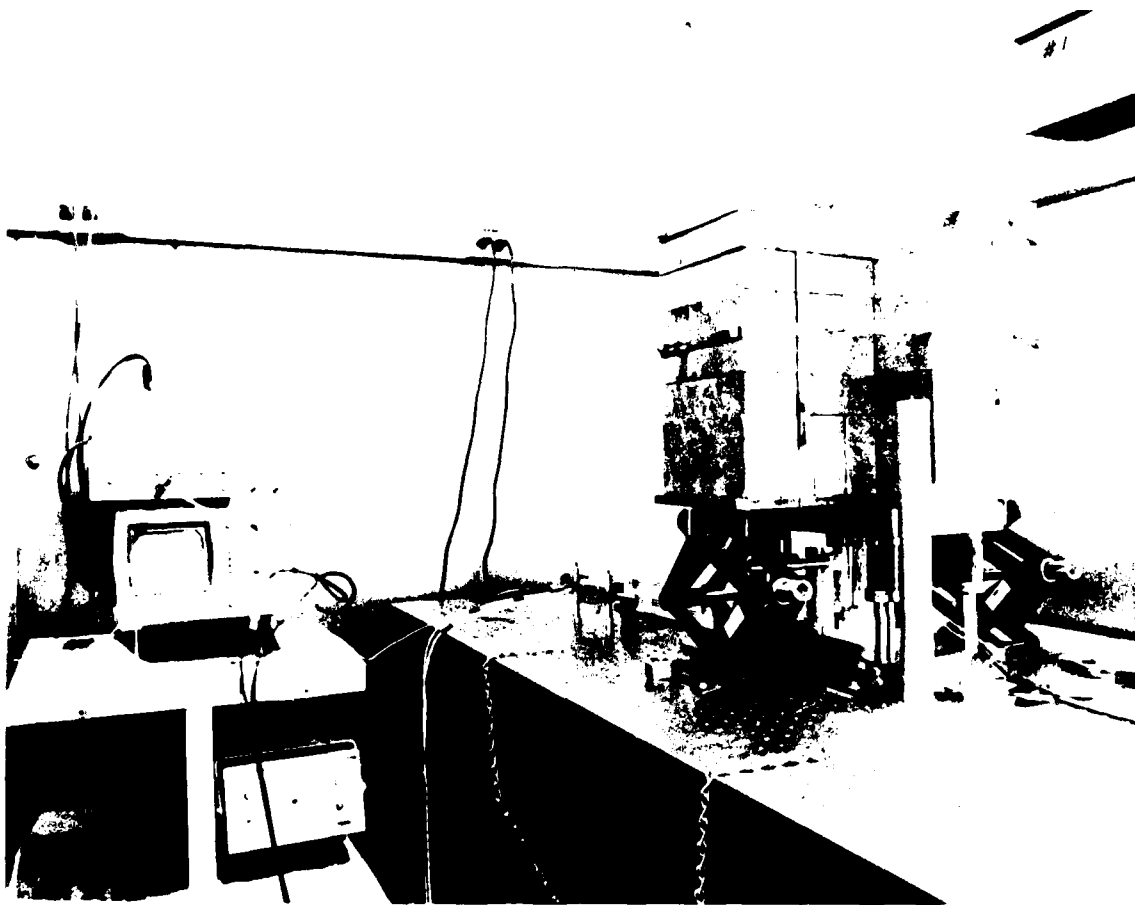


Figure 5. Photograph of new creep test system showing lead-brick loading system and modulated photodetector output signals.

III. DESIGN OF A NEW SYSTEM

A. LOAD APPLICATION

Fluctuations of an applied load will lead to apparent strain measurement errors. For example, a change of 0.4 lb will produce an elastic deformation of over 0.1 microstrain in a material with a Young's modulus of 20×10^6 (twice as stiff as aluminum) and a 0.5-in. diameter. Hydraulic presses that could maintain loads to within 0.5 lb for over 2500 hr were not available. Deadweight loading was considered to be essential.

Because a tensile loading creep frame fixture can be unstable (see Section II.B), a new scheme was devised. It consisted of placing lead bricks on a steel fixture comprising ball-bearing-guided support rods. Figure 5 shows the bricks and the fixture placed over a 5-in.-long rod sample surrounded by an aluminum (Al)-wrapped heating tape. Jacks are in place to remove or apply the load. The loading fixture sits on a floating-air table (Fig. 5) intended to minimize vibrations transmitted from the floor. It was not possible to utilize the compressed-air feature of the table, however: The lead bricks raised the table's center of gravity enough to cause instability in the automatic height-control pneumatic servo system. The ensuing table motions caused distortions in the table top and thus in the optical beam paths. An effort to lower the center of gravity with weights suspended by chains (see Fig. 5) was unsuccessful. A larger table may suffice. In this work the combination of rubber mounts and resistance-capacitance (R-C) damping circuits for the interferometer signals prevented vibration effects.

B. OPTICAL SYSTEM

We developed a unique optical scheme, based on the Michelson interferometer, to follow relative motion of the sample end faces and hence sample deformation (Fig. 6). The interferometer measures the change in the optical pathlength difference or

$$\text{OPLD} = 2n_1(\overline{abcd}) - 2n_2(\overline{aef}) \quad (1)$$



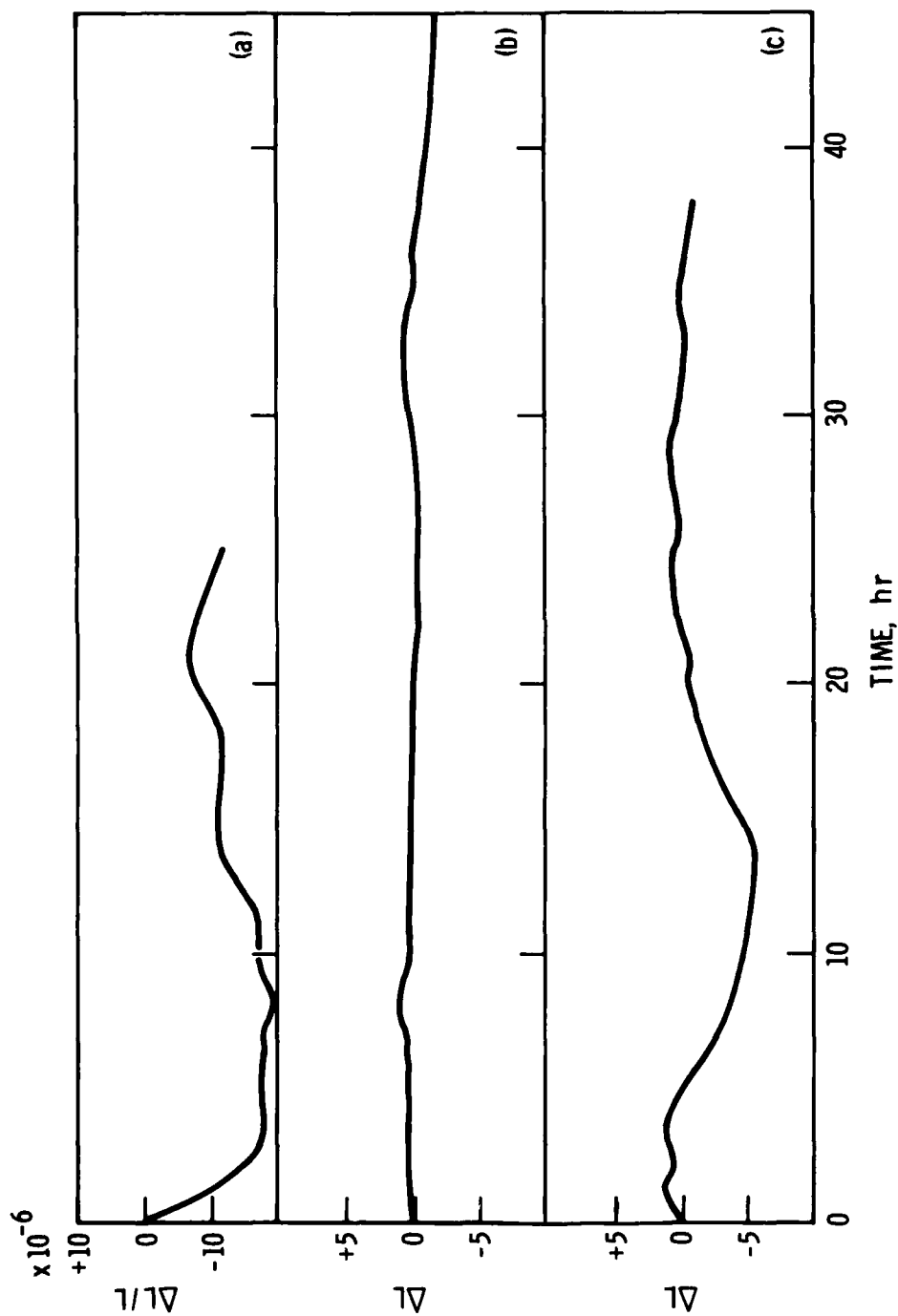


Figure 4. (a) Stability data for the creep test arrangement of Figure 3, with a pressure of 6000 psi on a 5-in.-diam alumina rod. (b) Stability data when both mirrors (D and B) were mounted on top plate during compression test. (c) Stability data when both mirrors (D and B) were mounted on lower sample support plate. Results indicate lower plate is unstable with time when load is applied.

Minimization of optical errors is only part of the task in a creep test. The mechanical loading and optics support systems must also be stable to at least an order of magnitude smaller than the expected sample strains. Stability tests of the creep frame of Figure 3 were carried out with various optics arrangements and a 6000-psi compressive load on an alumina rod. Figures 4a, b, and c show the drift of the complete system with sample, and the upper and lower platens only. The figure indicates that the lower-sample support plate in Figure 3 lacked microinch stability for periods longer than 5 to 10 hr. The degree of tolerance and friction of the center plate support rods through the top fixture plate may explain that instability. The apparatus of Figure 3 was therefore considered unsatisfactory.

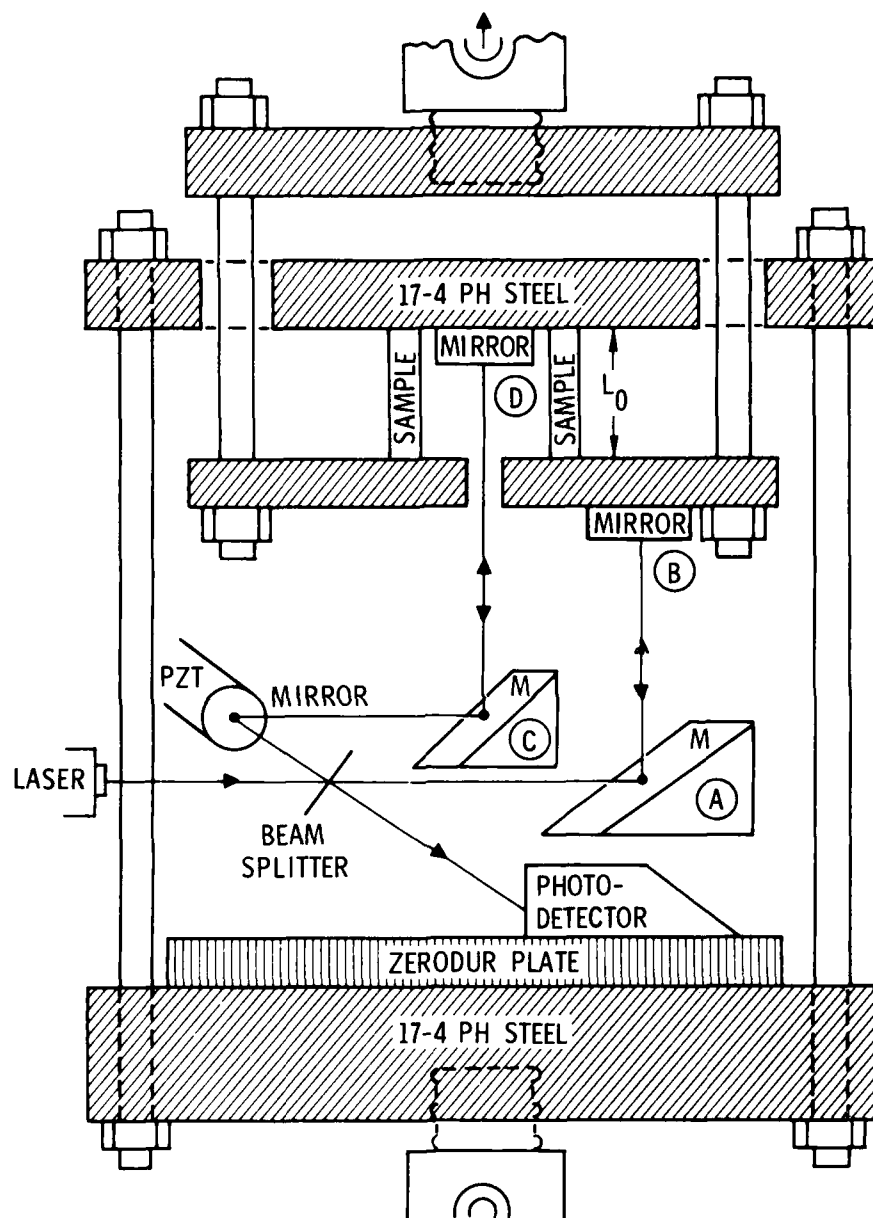


Figure 3. Indirectly loaded compression creep fixture with a Michelson interferometer strain transducer. A and C are beam-steering mirrors to the two mirrors B and D, respectively, mounted near each end of the tubular sample of length L_0 .

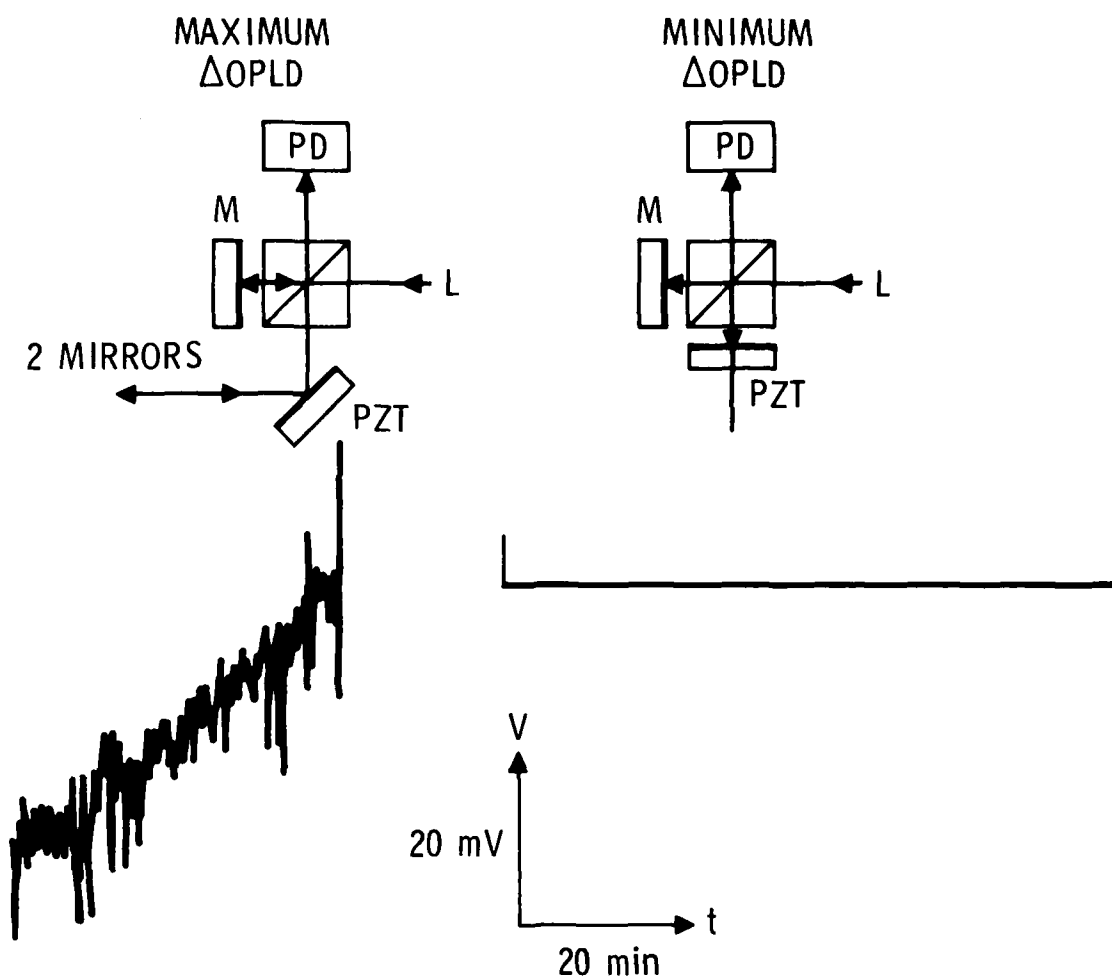


Figure 2. Effect of optical pathlength difference (OPLD) on the stability in air of a Michelson interferometer. Since $\text{OPLD} = n(L_1 - L_2)$, where L 's are the geometrical arm lengths, changes in OPLD (the interferometer output) disappear as L_1 approaches L_2 when n changes.

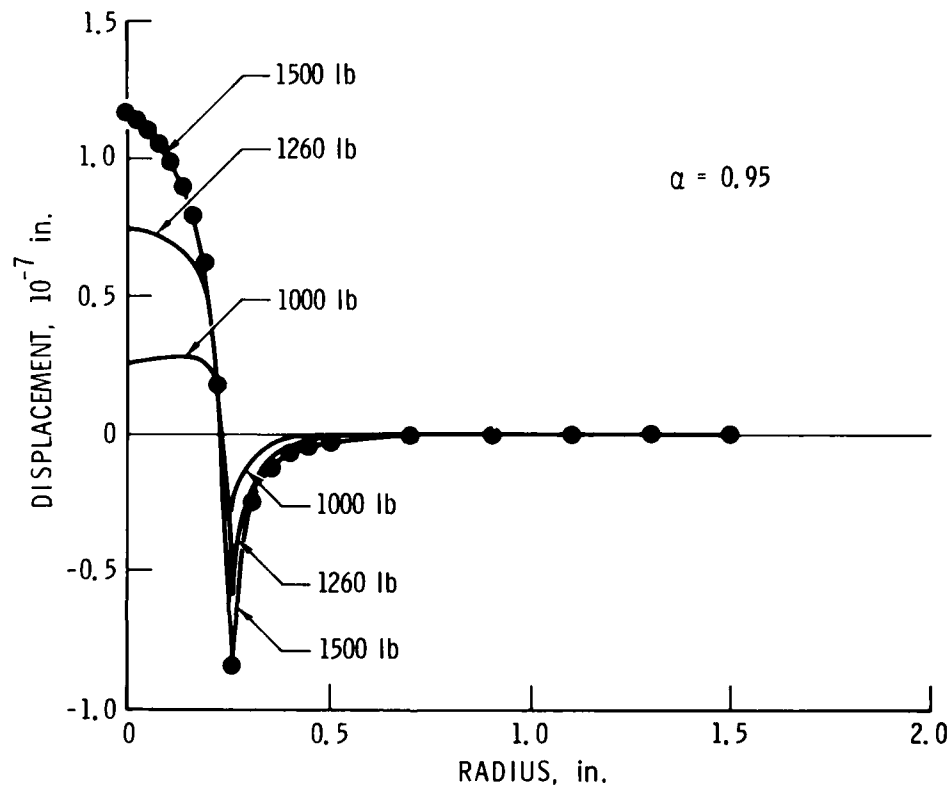


Figure 10. Displacement difference between elastic and inelastic analyses for the cylinder-substrate-steel plate interaction under normal load ($\alpha = 0.95$).

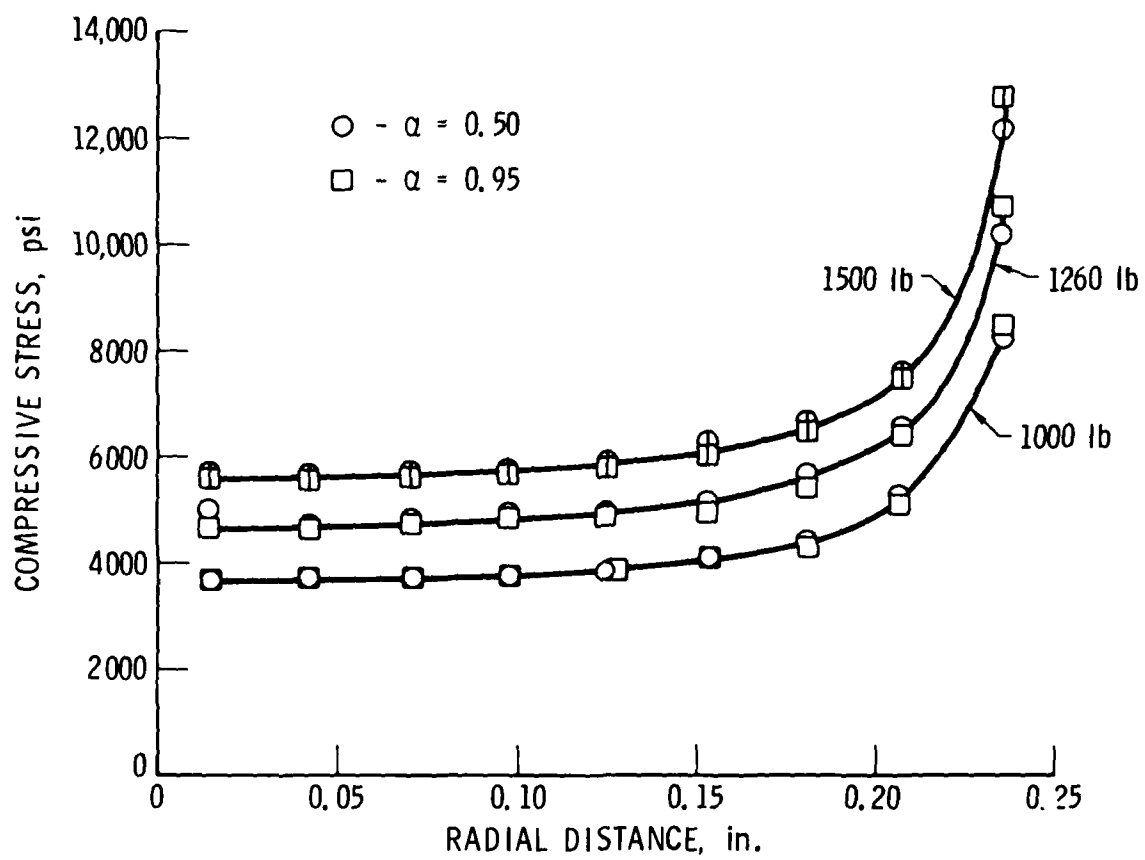


Figure 11. Compressive stress at specimen-plate interface.

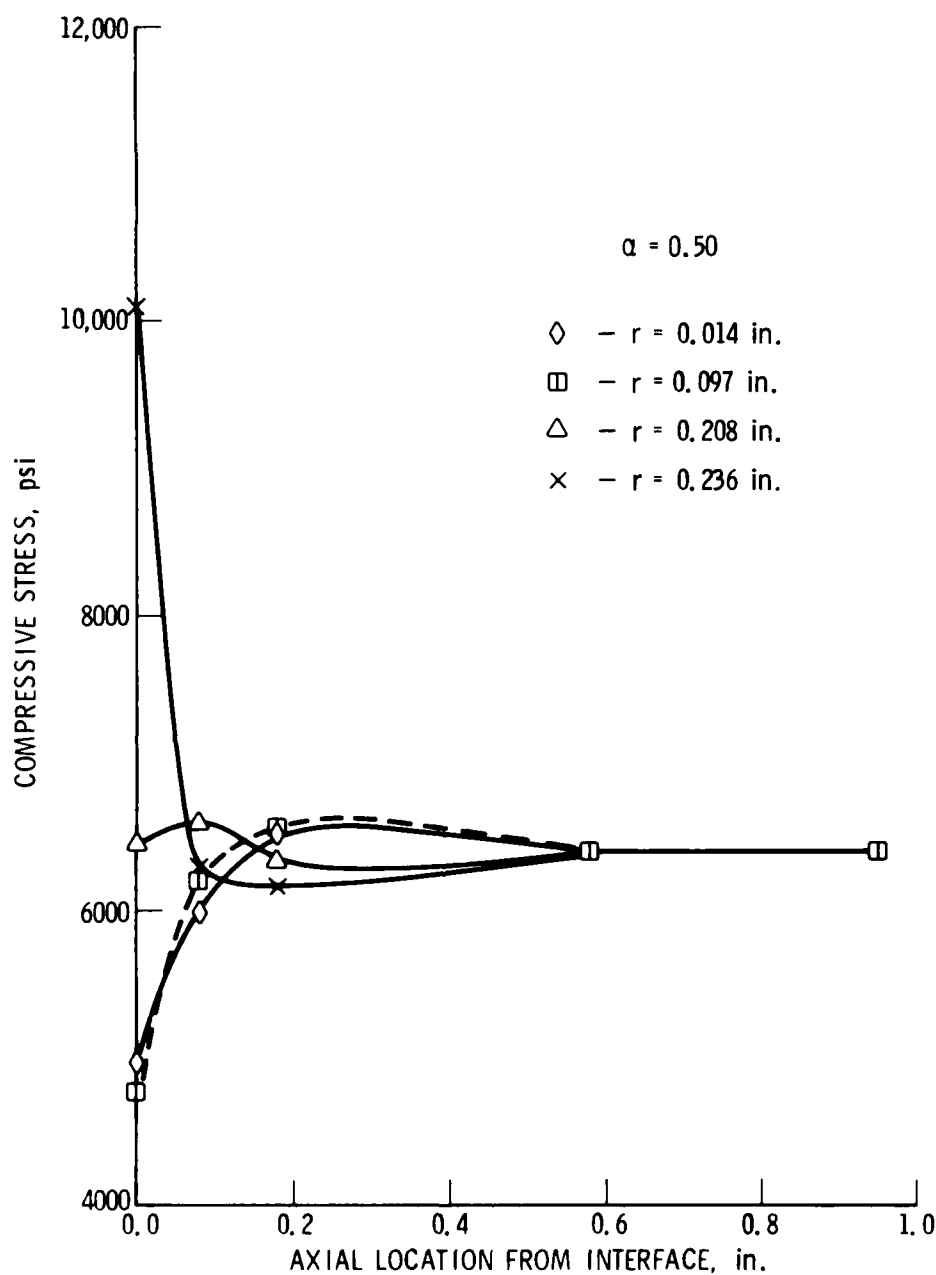


Figure 12. Normal compressive stress as a function of axial location (with $\alpha = 0.5$). The highest stresses at interface also occur near the sample edge. (See Figure 11.)

Table 1. Summary of Cylinder-Substrate-Steel Plate Interaction under Normal Load

	1000 lb			1260 lb			1500 lb		
	Elastic	Inelastic $\alpha = .95$	Inelastic $\alpha = .50$	Elastic	Inelastic $\alpha = .95$	Inelastic $\alpha = .50$	Elastic	Inelastic $\alpha = .95$	Inelastic $\alpha = .50$
<u>Longitudinal Displacement</u>									
Center of Specimen, 10^{-4} in.	-0.8784577	-0.8787163	-0.881589	-1.106857	-1.107601	-1.115039	-1.317676	-1.318839	-1.329684
Edge of Specimen, 10^{-4} in.	-0.6998473	-0.6995824	-0.6967006	-0.8818013	-0.8812031	-0.874628	-1.049755	-1.048907	-1.039712
<u>Displacement Difference with Elastic Case, in.</u>									
Center of Specimen	-	2.586×10^{-8}	3.1313×10^{-7}	-	7.44×10^{-8}	8.18×10^{-7}	-	1.163×10^{-7}	1.2008×10^{-6}
Edge of Specimen	-	-2.594×10^{-8}	-3.1417×10^{-7}	-	-5.982×10^{-8}	-7.173×10^{-7}	-	-0.848×10^{-7}	-1.0043×10^{-6}
0.5 in. from Specimen	-	-8.5×10^{-10}	-1.042×10^{-8}	-	-2.02×10^{-9}	-2.407×10^{-8}	-	-2.82×10^{-9}	-3.168×10^{-8}
1.5 in. from Specimen	-	-6.7×10^{-11}	-9.09×10^{-11}	-	8.7×10^{-11}	1.253×10^{-9}	-	-4.24×10^{-10}	7.397×10^{-9}
Normal max. stress, psi	-8483.65	-8460.00	-8197.3	-10,689.4	-10,638.55	-10,689.4	-12,725.45	-12,664.85	-12,074.95
σ^* , psi	6556.7	6507	5969.2	8261.3	8161.2	7117.7	9834.8	9704.3	8360.4
ϵ^* , %	0.04098	0.04116	0.04337	0.05163	0.05205	0.05772	0.06146	0.06215	0.07325
Inelastic Strain, 10^{-3} %	-	0.185	2.380	-	0.414	6.087	-	0.739	11.78

NOTE: σ^* = effective stress; ϵ^* = effective strain.

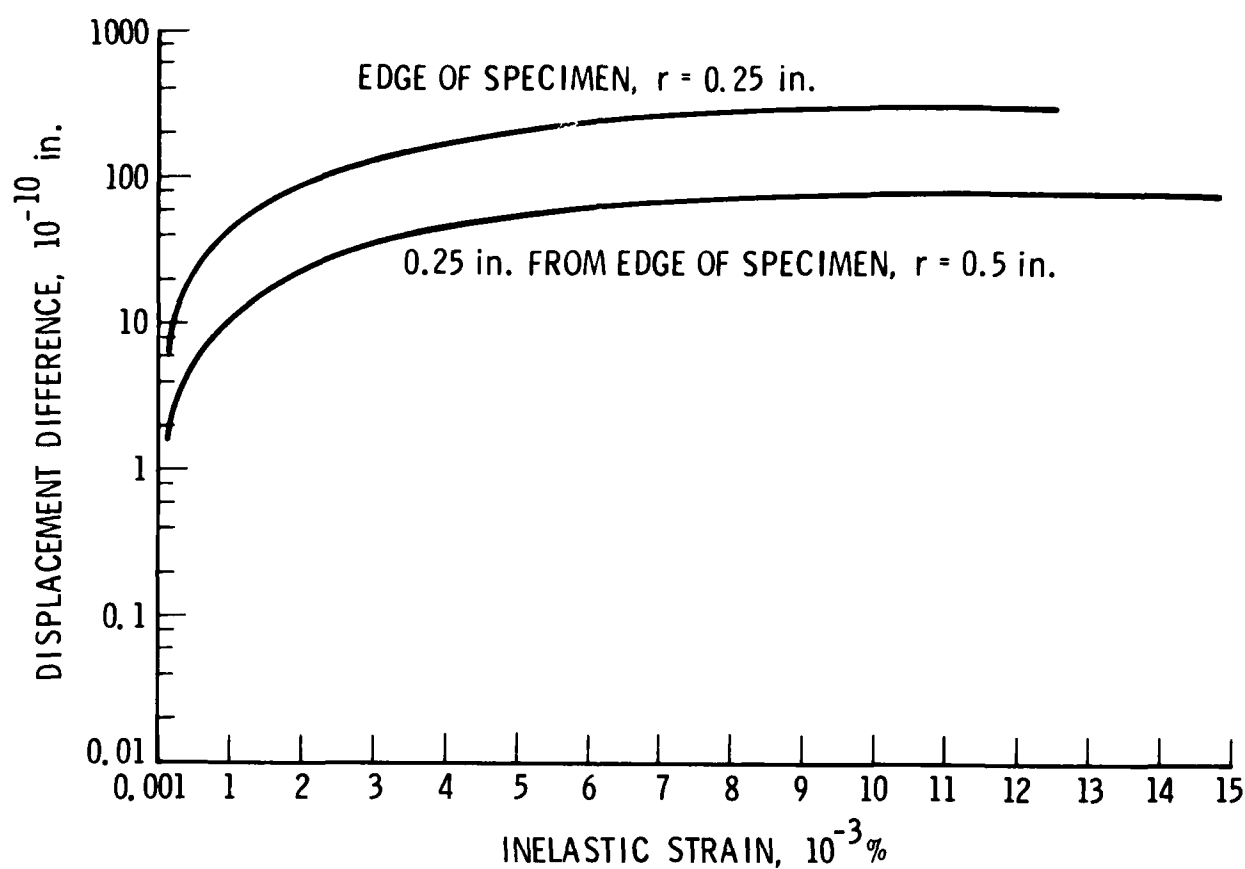


Figure 13. Displacement difference between elastic and inelastic cases versus the inelastic strain. The top curve represents this relation at the edge of the sample ($r = 0.25$); the lower curve represents the relation 0.25 in. from the edge of the specimen at the reflective steel plate surface.

difference at the specimen edge. Also, the displacement difference for the largest inelastic strain expected ($11.78 \times 10^{-3}\%$ from Table 1) is only 3×10^{-8} in. (the difference of the two curves in Figure 13), which is negligible.

2. ASYMMETRICAL LOADING

The difficulty in positioning the center of gravity of the lead bricks and their loading platform directly above the centerline of the sample gave rise to the possibility of nonuniform or asymmetrical loading. Such a possibility implied that the high edge stresses will rise at one side and the average stress in a radial direction will also increase on one side of the sample. The sample loading procedure required (a) using the laboratory jack to lower the steel fixture plate (with roller bearing sleeves) onto the sample and top alumina reflector plate, (b) lowering one side of the steel-plate-supporting lead bricks, and (c) lowering the other jack-supporting lead bricks. The two jacks shown in Figure 5 were alternately, rather than simultaneously, lowered. This meant that when the steel plate supporting the lead bricks made contact with the sample and the mirrored disk it supported, the steel loading plate was not exactly horizontal or parallel to the sample end face. Friction during final load application would then result in asymmetrical axial loads in the sample.

To check this hypothesis experimentally, we mounted two identical strain gages on opposite sides at the center of an identical pure Al rod sample and affixed them with a room-temperature curing adhesive. The strain gage electronics were stabilized for 2 hr at 19.3°C , the test temperature. The total weight of 1236 lb was applied by lowering the rear jack first. This procedure was repeated several times while rotating the sample 90 deg each time. The test results are plotted in Figure 14; stress was calculated from the measured strains and assuming $E = 10 \times 10^6$ psi. The maximum deviation for a uniform strain is $\sim 80 \mu\epsilon$ or $\sim 13\%$ of the average value.

The data also reveal that the side nearest the first load application receives the highest final stress value. The stresses along the interface of a rigid cylindrical punch with an elastic material when the punch is asymmetrically loaded are given by Muki¹² as

$$\left[\frac{\sigma_z}{2\mu} \right]_{z=0} = \frac{-\delta/a}{(1-\nu)\pi} \frac{1}{(1-\rho)^{1/2}} \left[1 + 2\left(\frac{\epsilon}{\delta}\right) \rho \cos \theta \right] \quad (4)$$

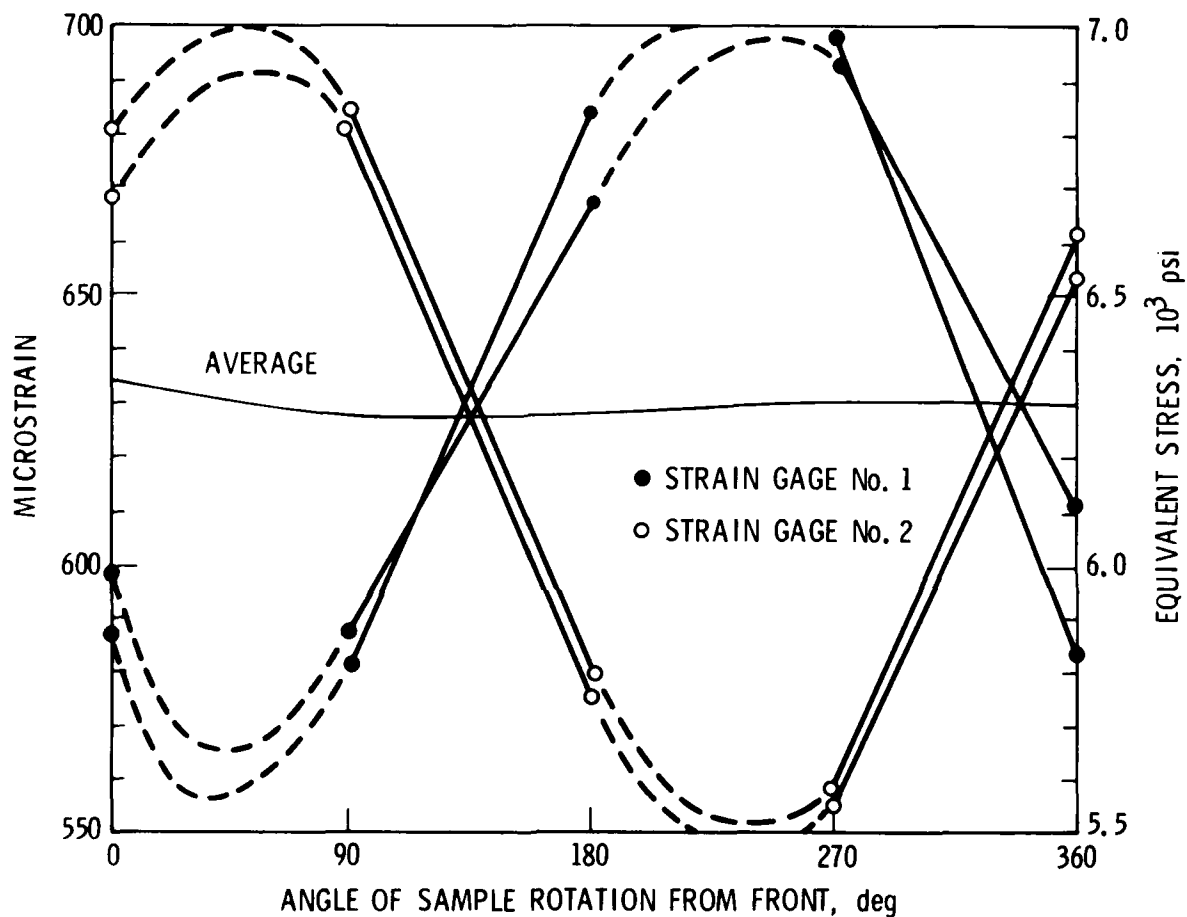


Figure 14. Strain readings from strain gages mounted 180 deg apart on a 0.5-in.-diam Al rod under 1236-lb axial compressions. The rod was rotated 90 deg between successive loadings. Strain gage No. 1 faced front at 0 deg.

where

σ_z = axial stress

δ = depth displacement

ϵ = displacement of edge compared with center of punch

μ = shear modulus

ν = Poisson ratio

a = punch radius

$\rho = r/a$, where r is the radial distance

z = axial distance along punch ($z = 0$ at punch end)

The compressive force P is related to the depth displacement δ by

$$P = \frac{-4a^2\mu}{1-\nu} \frac{\delta}{a} \quad (5)$$

For a 1260-lb load, the displacement δ in an alumina material from a rigid punch would be about 44 μ in. In Figure 14, we assume $\epsilon/\delta \sim 0.13$ (from the strain gage tests). The maximum axial stress asymmetry of the surface occurs at $\theta = 0$ deg ($\cos \theta = 1$). Figure 15 shows the asymmetry in axial stress at the sample-alumina interface for r varying from zero to $\pm a$.

Even without asymmetrical loading, the stress increases as $r \rightarrow a$, at least for $z/a \leq 1$. As long as $d\epsilon/dt = k\sigma$, there will be little error in asymmetrical loading as the average stress is maintained at all values $-a < r < a$. However, an increased stress region near the periphery may exceed the microyield strength (MYS) and faster creep rates apply, e.g., $\epsilon \propto \sigma^m t^n$.⁶

The creep rate or total creep strain is generally proportional to the stress level near or below the MYS stress. For example, Marshall and Maringer³ report that for 2024 and 6061 Al at 50 to 90% of the MYS, the creep strain at 1400 hr is proportional to the stress level. Consequently, one can draw isocreep rate regions for the top reflector plate (alumina). Because of

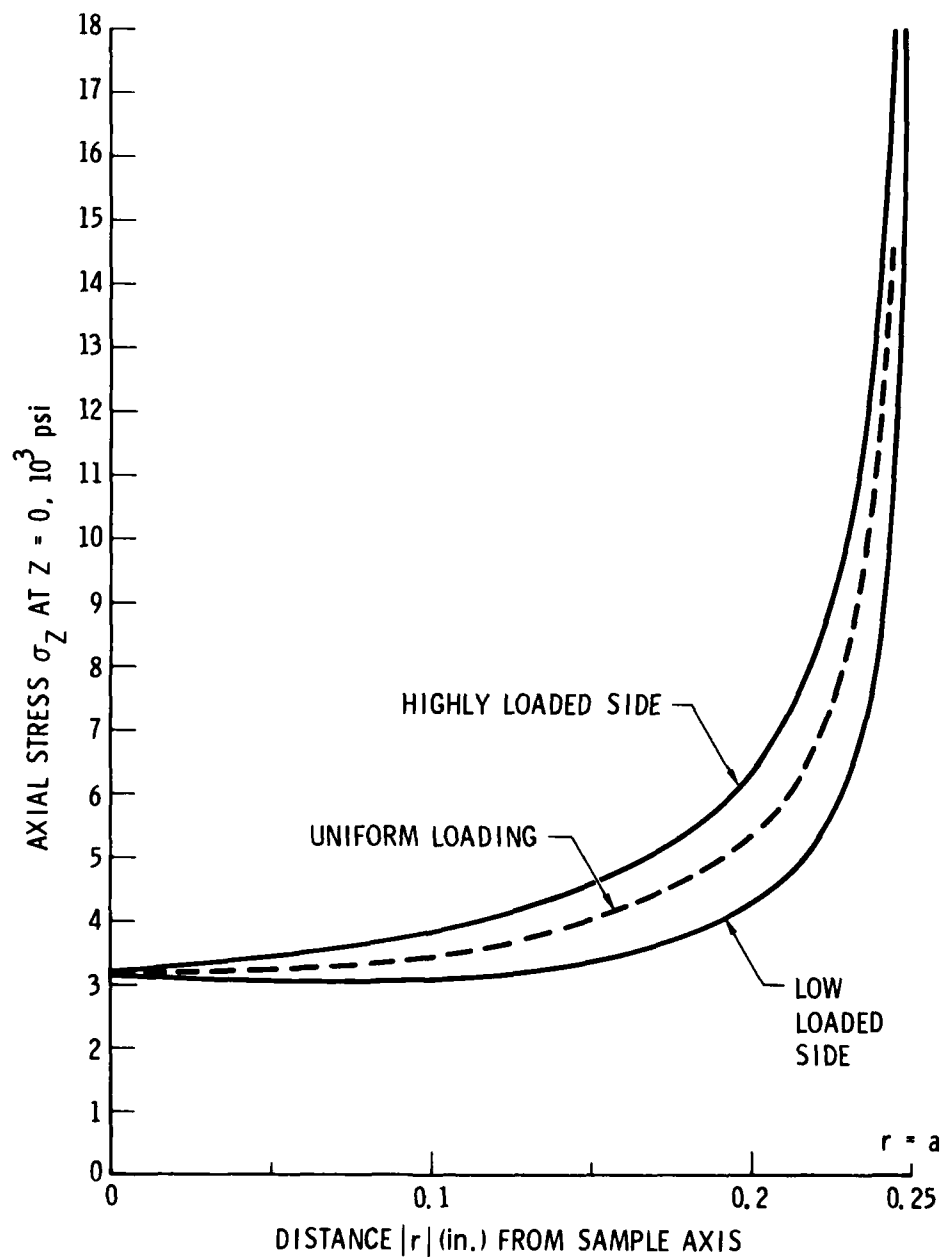


Figure 15. Maximum difference in surface σ_z for asymmetrically loaded model system ($\epsilon/\delta = 0.13$).

the forward position of the beam (point d in Fig. 6) and the high stresses toward the rear of the sample, one would not expect to measure a higher creep rate than the sample average, unless this loading procedure were variable. Creep test misalignment effects decrease with time and may also be minimized by using long test samples.¹³

C. SIGNAL-PROCESSING ERRORS

Strain measurement errors attributable to the signal-processing (S-P) system fall into two categories: (a) discontinuous changes in the fringe output count, and (b) nonlinearities caused by the method used for fringe interpolation. The first is caused by voltage spikes in the electrical system, resulting in instantaneous jumps in the output at integer multiples of the voltage equivalent to one count. These discontinuities can be detected by a chart recorder and be automatically deleted from the output data.

The method to count and interpolate between fringes has been described in detail elsewhere.^{9,14} Figures 5 and 6 show that the fringe pattern is reflected to an S-P beam splitter, which in turn sends the two orthogonally polarized beams to separate silicon photodetectors. The ellipse on the oscilloscope (Fig. 5) results from putting the two amplified signals (converted to voltage) on each axis of the scope and oscillating one of the beam paths (at b, Fig. 6) at 100 Hz by a PZT. The fringe movement is recorded by means of this oscillating signal. Once around the ellipse is equivalent to a $\lambda/2$ change in OPL difference in the interferometer. A directional quadrature counter records each zero crossing and counts the up or down changes in units of $\lambda/2$ (which are then converted into a 10-mV output signal). Interpolation within $\lambda/2$ is achieved by recording the duty cycle of each oscillation. The time spent at one or at zero counts is proportional to the position within a fringe. Interpolation to less than $\lambda/100$ can be achieved. The output is normally recorded to the nearest 0.01 mV on a data logger. The linearity of this counting scheme was tested by moving one reflecting mirror in the interferometer with a PZT, thereby simulating a sample length change. The signal-processor output depends on the orientation angle of the PZT as well as its voltage characteristics. Within a total ΔL of about 1000 Å the maximum

deviation from a straight line is about 30 Å. Further analysis would be required to determine whether these deviations result from optical effects, such as inadequate mode matching or wavefront errors,⁶ or from electronic counter nonlinearities.¹⁴

D. THERMAL ERRORS

Measurement errors may originate from nonuniform heating or cooling of (1) the lower steel plate, (2) the mirror plates, or (3) the optics supports, particularly the PZT-driven mirror support. Since only changes in temperature conditions would affect the creep results, a sample identical to the test sample is installed at test conditions both before the actual test begins and during any intermittent measurements such as gage block comparisons.

The stability of the system was measured for nearly 120 hr, using a 2-in. Zerodur test sample at room temperature and no load except that from the weight of the top steel mirror disk, equivalent to 0.5 psi. Optical path-lengths in air were made equal to within 0.1 in. The Invar holder for the steel tube supporting the PZT-driven mirror was bonded to a Zerodur block with Varian TORR-Seal epoxy resin. Apparent in Figure 16, a plot of the $\Delta L/L$ data taken at 15-min intervals with an HP-IL microprocessor system, is a daily temperature variation of about $\pm 0.4^\circ\text{C}$ and a sample strain fluctuation of about $\pm 30 \times 10^{-7}$. (The gaps in the strain curves can be attributed to the digital-to-analog converter and counting system when operated around the zero point.) The results are quantitatively explainable by temperature variations of the steel PZT holder:

$$\begin{aligned} \left(\frac{\Delta L}{L}\right)_{\text{apparent}} &= \frac{2L_s \alpha_s \Delta T}{L_z} = \frac{2(0.6)(11.4 \times 10^{-6})(\pm 0.4)}{2} \\ &= \pm 27.4 \times 10^{-7} \end{aligned} \quad (6)$$

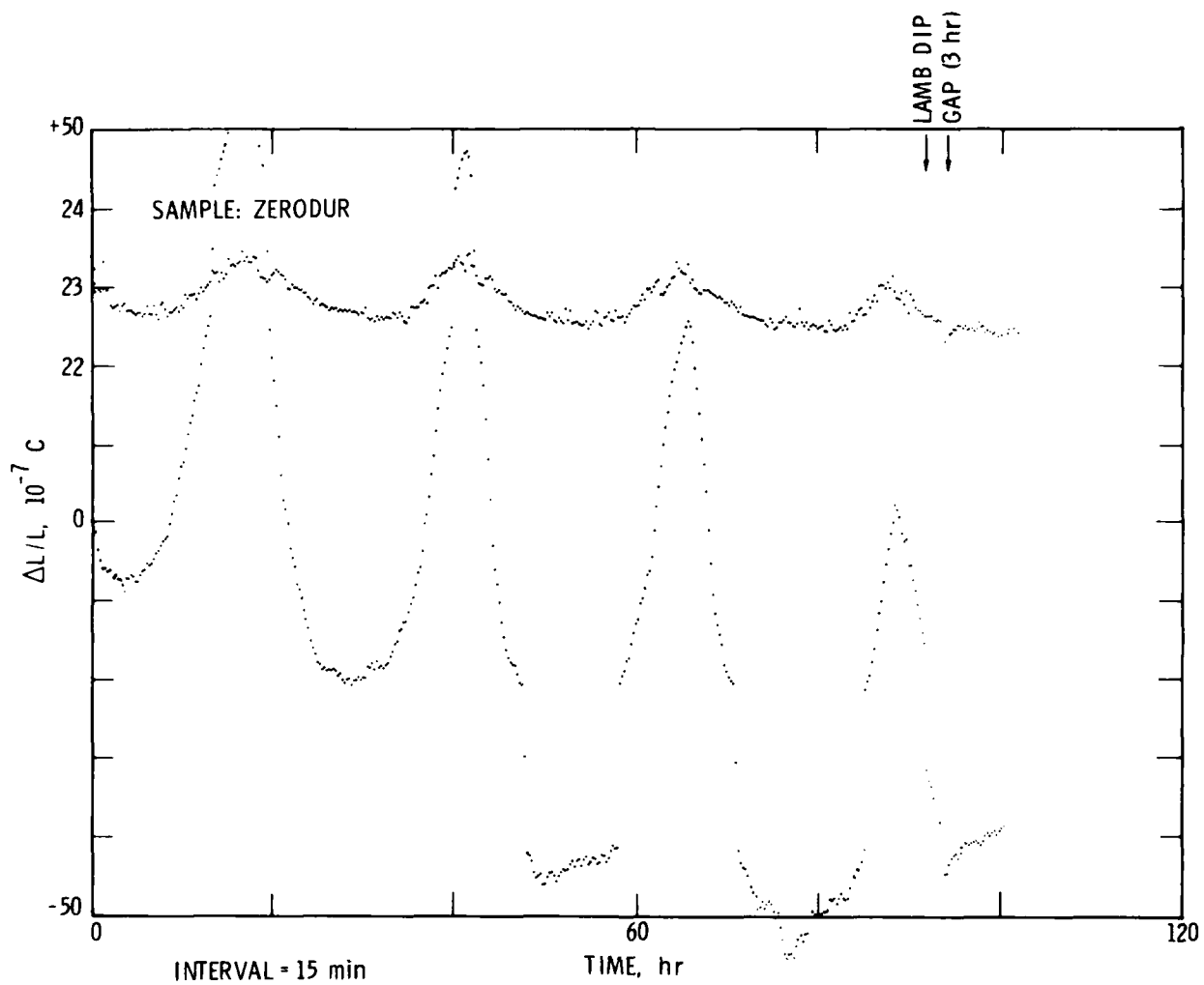


Figure 16. Temperature of Zerodur sample and apparent strain as a function of time with PZT-modulated mirror (point b in Figure 6).

Over a few hours, Lamb dip* control of the laser frequency, a method that leads to a frequency stability of 5 parts in $10^9/500$ hr, had no discernible effect on these results.

Replacement of the PZT with a ULE mirror bonded directly to the Zerodur block eliminated the automatic counting scheme. The recombined beams could still be analyzed with an S-P beam splitter and two photodetectors. Their quadrature signals, plotted in Figure 17, indicate a peak-to-peak voltage on each (about 4 V) that represents a displacement of $\lambda/2$. The relative phase displacement of the signals can be correlated with sample expansion or contraction. The figure demonstrates that, after an initial equilibration period, stability is within 0.5 V and fluctuations correspond to a Zerodur negative expansion coefficient of about $-0.15 \times 10^{-6} \text{ } ^\circ\text{C}^{-1}$, indicating that elimination of the steel-mounted PZT crystal has significantly improved the stability of the system to less than $10^{-7}/100$ hr. A signal-processing system based on the photodetector signals is being developed for plotting $\Delta L/L$ directly.

*A plot of beam intensity versus wavelength would give a double peak around the center wavelength of 632.8 nm. The Lamb dip is located by adjusting the laser cavity length to tune the frequency so that any deviation in either direction means an increase in output power. Such tuning is done by an automatic feedback mechanism that "hunts" for the minimum power at a search frequency of 12 kHz. Lamb dip is a consequence of the Doppler effect in gas lasers. See W. E. Lamb, Phys. Rev. 134, 1429 (1964).

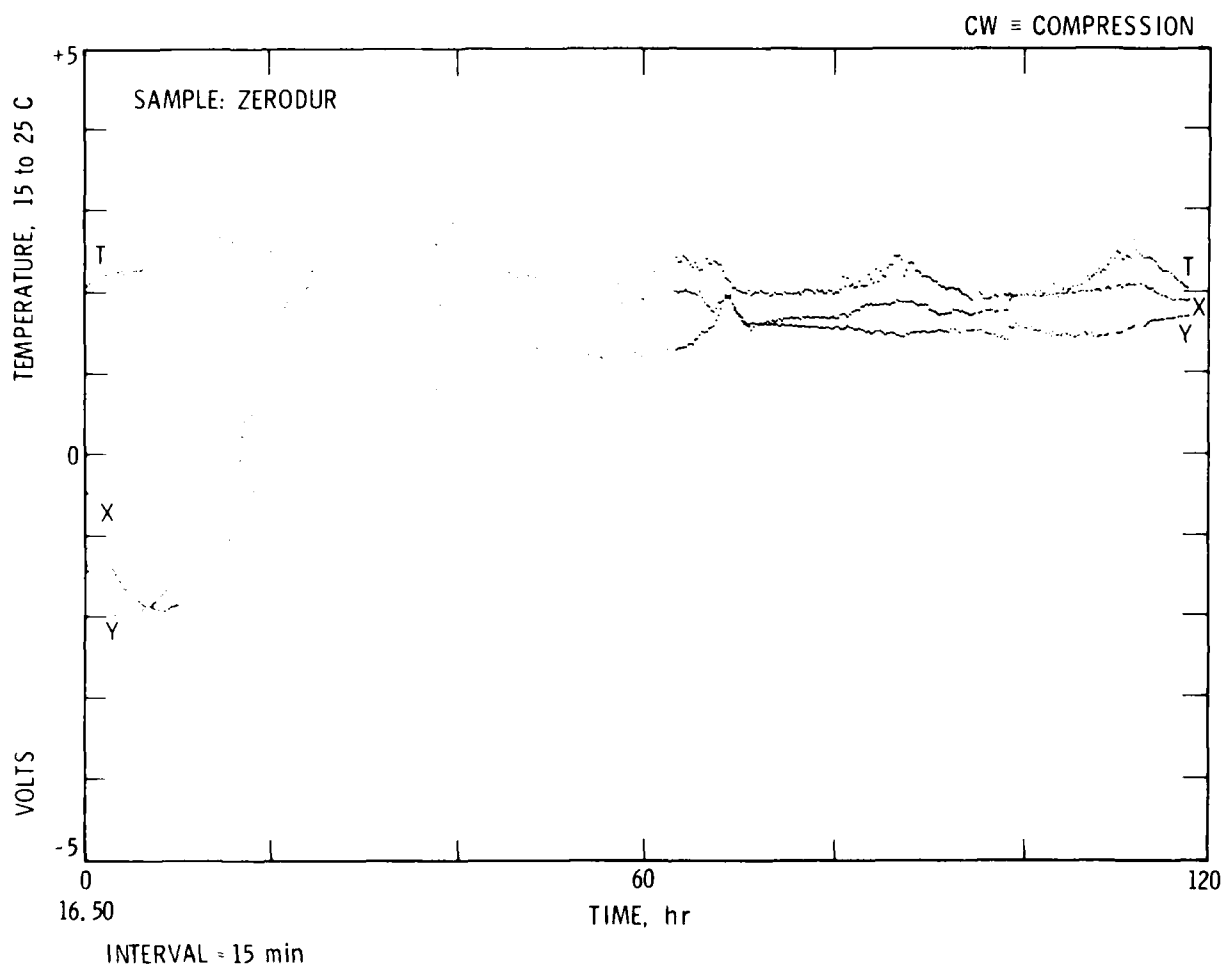


Figure 17. Temperature of Zerodur sample and apparent strain as measured by quadrature photodetector signals without a PZT-modulated mirror.

V. CONCLUSIONS

A new Michelson-interferometry-based technique for microcreep testing in air has been developed. It can be applied to a wide variety of temperature and (compressive) loading conditions, and may also be used for compressive microyield strength and temporal stability (no applied stress) measurements. The strain transducer elements can also be applied to tensile loading.

The stated objectives for compressive load range, sample temperature, and creep strain resolution and accuracy were met or exceeded. The sample measurement system can be dismantled in a few minutes for periodic, independent measurement of sample dimensions.

The voltage outputs of the interferometer signal-processing system can be automatically recorded by a data logger to 0.01 mV, corresponding to a $\lambda/2000$ ($10 \text{ mV} = \lambda/2$) sensitivity (or 0.012 $\mu\text{in.}$ or 3 \AA) for a HeNe laser source. If the photodetector signals are recorded directly, the sensitivity can be increased even further, since $4 \text{ V} = \lambda/2$. An improvement by a factor of 10 would mean a sensitivity of about 2 parts in 10^9 . Accuracy will be limited by vibration and use of the PZT modulator, which gave a value of $\pm 15 \text{ \AA}$, representing a strain accuracy of about 1.2 parts in 10^8 for samples 5 to 10 in. long.

The long-term stability was dominated by thermally induced errors in the optics supports, principally the support structure for the PZT-driven mirror. Elimination of all non-Zerodur or non-ULE glass optics supports evidences that stabilities close to 10^{-8} in strain measurements may be obtained for periods of at least 100 hr. Further improvements in the overall operation would include the following:

- Use of strain gages on the sample to ensure uniform load application.
- A large air-mounted table with a low center of gravity to minimize scatter from induced vibrations.
- Sample temperature control to less than 0.1°C .

- Automatic correction for sample temperature variations.
- Stabilization of the system with a dummy sample prior to the first load application.
- Within a modulated or counter system, phase interpolation based on polarization techniques should consider wavefront and related errors (see Ref. 6).

A bilinear inelastic finite-element analysis determined the magnitude of the displacement change due to creep at the interferometer measurement points (points d and f in Fig. 6). The results indicated that the displacement difference between elastic and inelastic cases increases with an increase in inelastic strain. The displacement difference can be represented as a function of inelastic strain only, the displacement approaching an infinitesimally small value when the radial distance is 0.25 in. from the edge of the specimen. The analysis was performed for steel plates; the use of higher-stiffness plate or disk mirrors would mean an even smaller effect on the accuracy of the creep measurement.

REFERENCES

1. C. S. Susskind and E. G. Wolff, The Measurement of Dimensional Stability of Invar Using Strain Gages, TR-0076(6950-07)-4, The Aerospace Corporation, El Segundo, Calif. (9 August 1976).
2. J. W. Lyons, Absolute Capacitance Microcreep and Dimensional Stability Measuring System, NASA Electronics Research Center Report C-134 (1970).
3. C. W. Marshall and R. E. Maringer, Dimensional Instability, Pergamon Press (1977).
4. E. G. Wolff, 9th National SAMPE Symposium, 4-6 October 1977, Vol. 9, Conf. Series (1977), pp. 57-72.
5. J. W. Berthold, S. F. Jacobs, and M. A. Norton, Appl. Opt. 15(8), 1898-1899 (1976).
6. R. Hochen and B. Justice, Dimensional Stability, NASA-CR-144162 (February 1976) (Contract No. NAS8-28662).
7. R. A. Paquin and W. R. Goggin, Micromechanical and Environmental Tests of Mirror Materials, Final Report on NASA Contract NAS5-11327, Perkin-Elmer Corp. (1971).
8. C. F. Bruce and R. M. Duffy, "Interferometric Techniques for Measuring Dimensional Stability of Passive Etalons," Appl. Opt. 9(3), 743-747 (March 1970).
9. S. A. Eselun, R. A. Savedra, and E. G. Wolff, Analysis and Design of a New Phase-Modulated Michelson Interferometer, TR-0082(2935-07)-1, The Aerospace Corporation, El Segundo, Calif. (18 December 1981).
10. J. C. Owens, "Optical Refractive Index of Air: Dependence on Pressure, Temperature, and Composition," Appl. Opt. 6(1), 51-59 (January 1967).
11. A. Wexler, Humidity and Moisture, Vol. III, Reinhold Publishing Company (1965), Chap. 1.
12. R. Muki, "Asymmetric Problems of the Theory of Elasticity for a Semi-Infinite Solid and a Third Plate," Advances in Solid Mechanics, 1st ed., N. Snedden (1957), Chap. VIII, pp. 401-439.
13. H. C. Wu and P. P. Wang, "Analysis of Test System Misalignment in the Creep Test," Trans. ASME 104, 280-284 (October 1982).
14. E. G. Wolff and R. C. Savedra, "Precision Interferometric Dilatometer," submitted to Rev. Sci. Instrum.

LABORATORY OPERATIONS

The Laboratory Operations of The Aerospace Corporation is conducting experimental and theoretical investigations necessary for the evaluation and application of scientific advances to new military space systems. Versatility and flexibility have been developed to a high degree by the laboratory personnel in dealing with the many problems encountered in the nation's rapidly developing space systems. Expertise in the latest scientific developments is vital to the accomplishment of tasks related to these problems. The laboratories that contribute to this research are:

Aerophysics Laboratory: Launch vehicle and reentry fluid mechanics, heat transfer and flight dynamics; chemical and electric propulsion, propellant chemistry, environmental hazards, trace detection; spacecraft structural mechanics, contamination, thermal and structural control; high temperature thermomechanics, gas kinetics and radiation; cw and pulsed laser development including chemical kinetics, spectroscopy, optical resonators, beam control, atmospheric propagation, laser effects and countermeasures.

Chemistry and Physics Laboratory: Atmospheric chemical reactions, atmospheric optics, light scattering, state-specific chemical reactions and radiation transport in rocket plumes, applied laser spectroscopy, laser chemistry, laser optoelectronics, solar cell physics, battery electrochemistry, space vacuum and radiation effects on materials, lubrication and surface phenomena, thermionic emission, photosensitive materials and detectors, atomic frequency standards, and environmental chemistry.

Electronics Research Laboratory: Microelectronics, GaAs low noise and power devices, semiconductor lasers, electromagnetic and optical propagation phenomena, quantum electronics, laser communications, lidar, and electro-optics; communication sciences, applied electronics, semiconductor crystal and device physics, radiometric imaging; millimeter wave, microwave technology, and RF systems research.

Information Sciences Research Office: Program verification, program translation, performance-sensitive system design, distributed architectures for spaceborne computers, fault-tolerant computer systems, artificial intelligence and microelectronics applications.

Materials Sciences Laboratory: Development of new materials: metal matrix composites, polymers, and new forms of carbon; nondestructive evaluation, component failure analysis and reliability; fracture mechanics and stress corrosion; analysis and evaluation of materials at cryogenic and elevated temperatures as well as in space and enemy-induced environments.

Space Sciences Laboratory: Magnetospheric, auroral and cosmic ray physics, wave-particle interactions, magnetospheric plasma waves; atmospheric and ionospheric physics, density and composition of the upper atmosphere, remote sensing using atmospheric radiation; solar physics, infrared astronomy, infrared signature analysis; effects of solar activity, magnetic storms and nuclear explosions on the earth's atmosphere, ionosphere and magnetosphere; effects of electromagnetic and particulate radiations on space systems; space instrumentation.

END

FILMED

6-85

DTIC